Electrically sign-reversible transverse g-factors of holes in droplet epitaxial GaAs/AlGaAs quantum dots under uniaxial stress

Yu-Nien Wu, Ming-Fan Wu, Ya-Wen Ou, Ying-Lin Chou, and Shun-Jen Cheng*
Department of Electrophysics, National Chiao Tung University, Hsinchu 30050, Taiwan, Republic of China
(Received 2 October 2015; revised manuscript received 12 July 2017; published 23 August 2017)

We present a theoretical investigation of anisotropic g-factor tensors of single holes confined in droplet epitaxial GaAs/AlGaAs quantum dots under electrical and mechanical controls using the gauge-invariant discretization method within the framework of four-band Luttinger-Kohn $\vec{k} \cdot \vec{p}$ theory. We reveal an intrinsic obstacle to realize the electrical sign reversal of the hole g-factors, being a key condition required for a full spin control in the scheme of g-tensor modulation, for the quantum dots solely with electrical bias control. Constructively, our studies show that, besides electrical gating, slightly stressing an inherently unstrained droplet epitaxial GaAs/AlGaAs quantum dot can offset the transverse hole g-factor to be nearly zero and make the electrical sign reversal of the hole g-factors feasible.

DOI: 10.1103/PhysRevB.96.085309

I. INTRODUCTION

Coherent and dynamical control over a single spin in a solid is a key feature required in spin-based quantum information processing [1,2]. In the past decade, various techniques have been developed in order to realize such a spin manipulation in solid-state nanostructures, including the application of continuous-wave oscillating magnetic field [3], the electrical tunings of exchange interaction [4], spin-charge couplings [5,6], and spin-orbital interactions [7–9], and also the electrical g-tensor modulation (g-TM) [10,11]. In particular, the electrical resonant or nonresonant g-TMs for holes in semiconductor QDs has persistently received increasing attention because of the advantages for the on-chip implementation [11–19] and the benefit from the long spin life and coherence times [19–22].

In the proposed nonresonant g-TM scheme of Ref. [11] a full spin control (FSC) over a carrier spin could be realized simply with the application of a static magnetic field and a local modulating electrical bias as long as the sign of a g-tensor component of the carrier can be electrically reversed. However, as reported by the most existing experiments it is technically quite challenging to make such an electrical sign reversal of g-factor for a spin carrier in semiconductor QDs. So far, with moderately high bias fields (∼tens of kV/cm) the g-tensor components for holes confined in QDs can be maximally varied by ∼60%, but the signs of the hole g-factors still cannot be reversed [12,14,15,19,23,24]. Until very recently, by driving the applied bias field onto the dots so high as $F > 200$ kV/cm Bennett *et al.* for the first time experimentally demonstrated the sign reversibility of the g-factors of valence holes confined in self-assembled InAs QDs [25]. The application of such an ultrahigh electrical bias control yet requires the delicate design of derivative barrier-layer structures to prevent the tunneling out of dot-confined carriers and is still uncommon in conventional electronics.

In this work, we theoretically study the g-factor tensors of single holes confined in intrinsically unstrained GaAs/AlGaAs quantum dots (QDs) [26], grown by droplet epitaxial (DE) techniques, under an electrical bias and uniaxial stresses within the four-band Luttinger-Kohn model in both numerical and analytical manners [27]. As compared with the more extensively studied strained InAs/AlGaAs QDs grown in the Stranski-Krastanov mode [28,29], GaAs/AlGaAs DE-QDs possess some unique advantageous features, including the free selection of substrate facet [30], flexible control of QD geometry [31–34], and the removal of complex inherent strain [35]. With the benefit from the unique material and nanostructure properties, advanced photonic devices such as single-photon and entangled photon sources have been successfully made of GaAs/AlGaAs droplet-epitaxial quantum dots (DE-QDs) [30]. Moreover, unlike strained InAs/AlGaAs QDs, inherently unstrained GaAs/AlGaAs DE-QDs that are sensitive to any slight external stresses [35,36] enable the use of mechanical stresses as an additional independent knob to electrical or magnetic fields for further tuning the material, electronic, and excitonic properties of QDs [36,37].

Numerically, we employ the gauge-invariant discretization method to calculate the spin-resolved energy levels of a hole confined in a QD with a static magnetic field, a uniaxial stress, and a tuning electrical bias [38–41]. For analysis of the numerical results, we take the 3D parabolic model for the QD confining potential and derive the formalisms of g-tensors of a QD-confined hole in terms of the stress- and electrically tunable dependent VBM. As a main result, our studies show that slightly stressing a DE-QD makes the required bias field for FSC over a hole spin dramatically drop by more than one order of magnitude, falling in the scales of voltage compatible to conventional electronics, and gets rid of the long standing obstacle for realizing the electrical g-TMR scheme. Though the main physics lying in a hole g-tensor is known related to the inherent valence band mixing (VBM), our analysis enables us to identify the components in the overall VBM that are in charge of sign reversibility of the resulting g-factors and find out the optimal means for control over them. Alternatively, the effect of stress on the spin-splitting of the hole energy levels of a QD with a hole can be regarded as an effective pseudomagnetic field that essentially involves the intrinsic spin-orbital coupling for $J = 3/2$ hole and directly coupled to the hole spin itself. Analogs between mechanical stress and pseudomagnetic field have been also made for other emergent materials with stresses, e.g., graphenes [42] and silica photonic crystals [43].

*Corresponding author: sjcheng@mail.nctu.edu.tw

This article is organized as follows. Section II presents the theoretical framework and the methodology for the calculations of hole g-tensors of DE-QDs with external electric fields and uniaxial stresses. Section III presents the numerically calculated results, including the magnetospectra of single holes in DE-QDs, and the anisotropic g-tensor components versus the applied electric fields and stresses. In Sec. IV, a model analysis based on the three-dimensional (3D) parabolic model is carried out for gaining physical understandings of the numerical results, and explicitly derives the conditions for the sign reversibility of hole g-factors of QDs, and predicts the feasibility of g-tensor modulation scheme for full coherent control over a hole spin in a DE-QD with appropriate uniaxial stresses. Section V concludes this work.

II. THEORETICAL FRAMEWORK

Within the four-band Luttinger-Kohn (LK) $\vec{k}\cdot\vec{p}$ model, the Hamiltonian for a $J=\frac{3}{2}$ valence hole confined in a DE-QD with a magnetic field $\vec{B}$, an electric field $\vec{F}$, and an external stress σ_s is expressed as a 4×4 matrix,

$$H_h = H_k^h + H_\epsilon^h + V_{\rm QD}^h I_{4\times 4} + H_Z^h + H_F^h, \tag{1}$$

composed of the kinetic energy, strain, QD potential, spin-Zeeman, and Stark-effect parts, respectively,

In the basis of Bloch functions ordered by $\{u^h_{j_z=3/2}, u^h_{j_z=1/2}, u^h_{j_z=-1/2}, u^h_{j_z=-3/2}\} \equiv \{|\Uparrow\rangle, |\uparrow\rangle, |\downarrow\rangle, |\Downarrow\rangle\}$, the Hamiltonian of kinetic energy is expressed by

$$H_k^h = \begin{pmatrix} P_k+Q_k & -S_k & R_k & 0 \\ -S_k^\dagger & P_k-Q_k & 0 & R_k \\ R_k^\dagger & 0 & P_k-Q_k & S_k^\dagger \\ 0 & R_k^\dagger & S_k^\dagger & P_k+Q_k \end{pmatrix}, \tag{2}$$

where $P_k = \frac{\hbar^2\gamma_1}{2m_0}(k_x^2+k_y^2+k_z^2)$, $Q_k = \frac{\hbar^2\gamma_2}{2m_0}(k_x^2+k_y^2-2k_z^2)$, $R_k = \frac{\sqrt{3}\hbar^2}{2m_0}[-\gamma_3(k_x^2-k_y^2)+2i\gamma_2\{k_x,k_y\}]$ and $S_k = \frac{\sqrt{3}\hbar^2\gamma_3}{m_0}(\{k_x,k_z\}-i\{k_y,k_z\})$, $\vec{k} = -i(\vec{\bigtriangledown}_{\vec{r}} + i\frac{e}{\hbar}\vec{A}) \equiv -i\hat{\vec{D}} = -i(\hat{D}_x, \hat{D}_y, \hat{D}_z)$ is the wave vector operator, $\{k_i,k_j\} \equiv \frac{1}{2}(k_ik_j+k_jk_i)$, $\vec{r}=(x,y,z)$ is the coordinate position of carrier, $\vec{A}(\vec{r}) = \frac{1}{2}\vec{B}\times\vec{r}$ is the $\vec{B}$-induced vector potential in the symmetry gauge, $e>0(m_0)$ stands for the elementary charge (mass) of free electron, and $\gamma_1=7.1$, $\gamma_2=2.02$, and $\gamma_3=2.91$ are the Luttinger parameters for GaAs [44,45].

The strain Hamiltonian H_ϵ^h preserves the same form as Eq. (2), but with the replacements of the subscript and the operators by $k\to\epsilon$, $P_\epsilon = -a_v(\epsilon_{xx}+\epsilon_{yy}+\epsilon_{zz})$, $Q_\epsilon = -\frac{b}{2}(\epsilon_{xx}+\epsilon_{yy}-2\epsilon_{zz})$, $R_\epsilon = \frac{d}{2}(\epsilon_{xx}-\epsilon_{yy}) - i\sqrt{3}b\epsilon_{xy}$, and $S_\epsilon = -d(\epsilon_{xz}-i\epsilon_{yz})$, respectively, where $\{\epsilon_{ij}\}$ are the strain tensor elements, and the strain parameters for GaAs are $a_v=1.16$ eV, $b=-1.7$ eV, and $d=-4.55$ eV [45]. In this work, we consider asymmetric QDs on (001) substrate and elongated along the crystalline axis of $[1\bar{1}0]$, and specify the growth (elongation) axis as the z (x) axis, as depicted in Figs. 1(a) and 1(b). Applying a uniaxial stress of magnitude σ_s along the x axis yields the strain tensor elements, $\epsilon_{xx} = [\frac{1}{2}(s_{11}+s_{12})+\frac{1}{4}s_{44}]\cdot\sigma_s$, $\epsilon_{yy} = [\frac{1}{2}(s_{11}+s_{12})-\frac{1}{4}s_{44}]\cdot\sigma_s$, $\epsilon_{zz} = s_{12}\cdot\sigma_s$, and $\epsilon_{xy}=\epsilon_{xz}=\epsilon_{yz}=0$, where $s_{11}=0.0082$ GPa^{-1}, $s_{12}=-0.002$ GPa^{-1}, and $s_{44}=0.0168$ GPa^{-1} are the elastic compliances [45]. The third term in Eq. (1), $V_{\rm QD}^h I_{4\times4}$, is yielded by the confining potential, $V_{\rm QD}^h(\vec{r})$, of QD for a hole, where $I_{4\times4}$ stands for a 4×4 identity matrix.

Following the theory of Flatté *et al.* [38], the common effective Zeeman κ and q terms in Luttinger-Kohn $k\cdot p$ theory for semiconductor bulks are disregarded in Eq. (1) for QDs because of the revealed orbital quenching effect in QDs. Instead, the bare spin Zeeman term for $J=\frac{3}{2}$ is included in Eq. (1), which is given by

$$H_z^h = -\frac{2}{3}\mu_B\vec{B}\cdot\vec{J} = -\mu_B\begin{pmatrix} B_z & \frac{1}{\sqrt{3}}B_- & 0 & 0 \\ \frac{1}{\sqrt{3}}B_+ & \frac{1}{3}B_z & \frac{2}{3}B_- & 0 \\ 0 & \frac{2}{3}B_+ & -\frac{1}{3}B_z & \frac{1}{\sqrt{3}}B_- \\ 0 & 0 & \frac{1}{\sqrt{3}}B_+ & -B_z \end{pmatrix}, \tag{3}$$

where $\vec{B}=(B_x,B_y,B_z)$, $B_\pm \equiv B_x \pm iB_y$, and μ_B is Bohr magneton. The last Stark term is given by $-eFzI_{4\times4}$, in the envelope function approximation, for a vertical bias field $\vec{F}=(0,0,F)$ acting on a QD.

Within the four-band model, the ith single-hole eigenfunction is expressed as $|\psi_i^h\rangle = \sum_{\chi=\Uparrow,\uparrow,\downarrow,\Downarrow}|f_{i,\chi}^h\rangle|\chi\rangle$ that is composed of the slowly varying envelope functions, $f_{i,\chi}^h(\vec{r}) = \langle\vec{r}|f_{i,\chi}^h\rangle$, and the microscopic Bloch functions of hole pseudospin $j_z=\frac{3}{2},\frac{1}{2},-\frac{1}{2},-\frac{3}{2}$, denoted by $\chi=\Uparrow,\uparrow,\downarrow,\Downarrow$, respectively, and satisfies the equation $H_h|\psi_i^h\rangle = E_i^h|\psi_i^h\rangle$.

III. NUMERICAL METHOD AND RESULTS

In the numerical studies, we consider asymmetric GaAs/$Al_{0.35}Ga_{0.65}$As DE-QDs shaped by Gaussian-function profiles, according to the observations of atomic force microscope [31,32,46], described by the characteristic function

$$X_{QD}(\vec{r}) = \begin{cases} 1, & 0\leqslant z\leqslant H\exp\left(-\frac{x^2}{\Lambda_x^2}-\frac{y^2}{\Lambda_y^2}\right), \\ 0, & \text{elsewhere} \end{cases} \tag{4}$$

[as depicted by Figs. 1(a) and 1(b)], where H is the height of QD and Λ_x (Λ_y) is defined as the characteristic side length of QD in the x direction (y direction). Thus the confining potential for a hole in a QD is expressed as $V_{QD}^h(\vec{r}) = V_b^h\cdot(1-X_{QD}(\vec{r}))$, where $V_b^h=200$ meV is the potential barrier of the GaAs/$Al_{0.35}Ga_{0.65}$As QD for a valence hole [45]. Here, we assume the abrupt GaAs/AlGaAs band-edge offset, based on the fact that the degree of GaAs/AlGaAs composition intermixing is very small for the QDs grown in the droplet epitaxial mode, as evidenced by the measurement of cross-sectional scanning tunneling microscopy (X-STM) reported by Keizer *et al.* [46]. Numerically, the spin-resolved energy spectrum of a single hole in a QD with an arbitrary magnetic field is obtained by solving the four-band Schrödinger equation, $H_h|\psi_i^h\rangle = E_i^h|\psi_i^h\rangle$ based on Eq. (1),

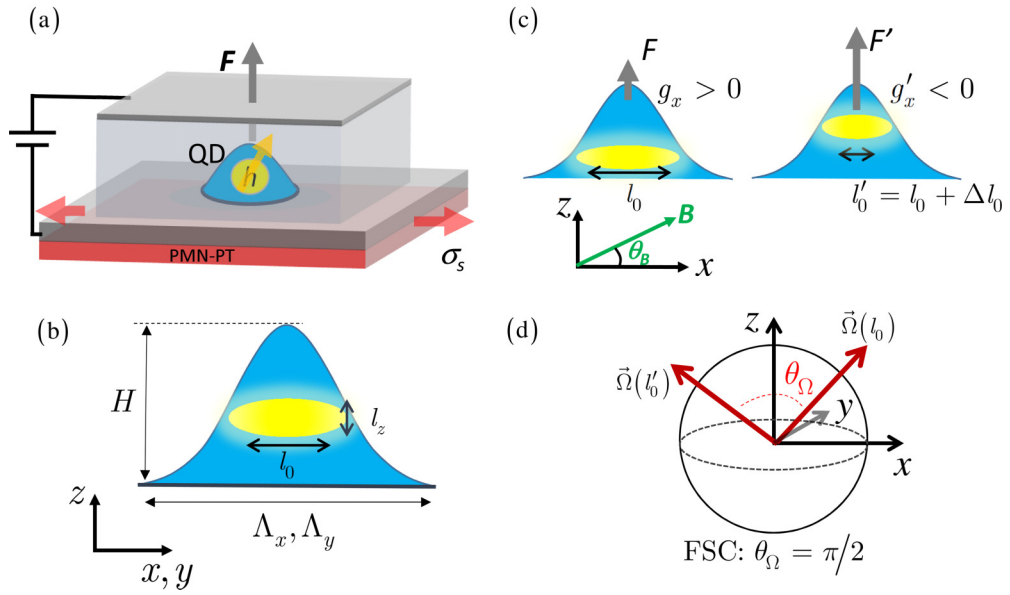

FIG. 1. (a) Schematics of a QD confining a valence hole under an electric bias field $\vec{F} = (0,0,F)$ and a uniaxial stress σ_s. (b) Schematics of a Gaussian-function shaped QD with the geometry parameters, H, Λ_x, and Λ_y [see Eq. (4) for the definitions]. In the parabolic model used in Sec. IV, the spatial extents of the QD-confined hole wave function along the α direction ($\alpha = x,y,z$) are characterized by the parameters l_α. With the neglect of the shape elongation of the QD, $l_0 \equiv \sqrt{l_x l_y}$ are defined to measure the averaged lateral extent of the hole wave function. (c) In an electrical g-TM scheme, a controlled bias field F is applied to the QD to tune the wave function extents and lead to the change of the g-tensor components with respect to a tilted magnetic field $\vec{B} = B(\cos\theta_B, 0, \sin\theta_B)$. (d) In the g-tensor modulation scheme, the F-driven change of g-tensor components is equivalent to the rotation, by an angle θ_Ω, of the effective field $\vec{\Omega}$ that is directly coupled to the hole spin. A full spin control (FSC) requires that $\theta_\Omega = \frac{\pi}{2}$.

using the gauge-invariant discretization method developed by Refs. [38–41] (see Appendix B for more details).

For an applied magnetic field $\vec{B}$ in an arbitrary direction, we define the hole g-factor of the QD as

$$g_h(\vec{B}) \equiv (E^h_{\Downarrow'}(\vec{B}) - E^h_{\Uparrow'}(\vec{B}))/\mu_B|\vec{B}|, \tag{5}$$

where $\Uparrow'$ ($\Downarrow'$) labels the lowest VBM hole state with the up-spin along (down-spin opposite to) the direction of the magnetic field. Following the definition, the longitudinal [transverse] component of g-tensor for a VBM hole in a QD is determined by $g_z = g_h(\vec{B} = (0,0,B))$ [$g_x = g_h(\vec{B} = (B,0,0))$ or $g_y = g_h(\vec{B} = (0,B,0))$] with respect to a vertical (in-plane) magnetic field.

Figure 2(a) [2(b)] presents the numerically calculated magnetoenergy spectra of an unbiased ($F = 0$) GaAs/AlGaAs QD of $H = 12$ nm, $\Lambda_x = 29.4$ nm, and $\Lambda_y = 19.6$ nm, under vertical [in-plane] magnetic fields and with different uniaxial stresses along the x direction. Figure 2(c) [2(d)] shows the corresponding g_z-factor [g_x-factor] of the VBM hole in the dot, as a function of σ_s, to the stress-dependent spin-split magnetospectra of Fig. 2(a) [Fig. 2(b)]. The values of the calculated longitudinal and transverse g-factors of a hole in the GaAs QD fall into the scales close to those measured by [47]. One sees that the longitudinal g_z-factor of the stressed QD remains roughly constant against the variation of the applied stress [see Fig. 2(c)] [48], while the transverse g_x-factor is shown stress sensitive [see Fig. 2(d)]. Remarkably, as the applied stress turns from compressive to tensile, the sign of g_x is switched from positive to negative and crosses over $g_x = 0$ at a tensile stress, $\sigma_s \sim 65$ MPa. As analyzed in more detail later, such a high stress tunability of the transverse g-factor is essentially associated with the stress-induced VBM of hole and is useful for realizing electrical sign reversibility of hole g-factor [11,25].

In Fig. 3, we present how an external electrical bias can be employed to tailor the spatial extents of a hole wave function of a QD, which will be shown essential in the electrical tunability of the underlying VBM and the resulting g-tensors by later analysis. Figure 3(a) shows the numerically calculated lateral and vertical wave function extents, $l_0^{\rm num}$ and $l_z^{\rm num}$ [defined in terms of the spatial standard deviations of wave function, $l_\alpha^{\rm num} \equiv \sqrt{2}\sigma_\alpha$, where $\sigma_\alpha = \sqrt{(\langle\alpha^2\rangle - \langle\alpha\rangle^2)}$ for $\alpha = x,y,z$, and $l_0^{\rm num} \equiv \sqrt{l_x^{\rm num} l_y^{\rm num}}$] for the major HH component of the lowest HH-like state of the QD considered in Fig. 2 under a vertical bias field varied from $F = -30$ to $+30$ kV/cm. The lateral extent of the hole wave function, $l_0^{\rm num}$, for the tall asymmetric QD (lacking of the up-down mirror symmetry) is well F-tunable, while the $l_z^{\rm num}$ is shown not so sensitive to the variation of F. Figure 3(b) shows the significant relative variation of the lateral extent of the major-HH and secondary-LH envelope wave functions over a wide range of $\Delta l_0^{\rm num}/l_0^{\rm num} = \{-20\%, +20\%\}$ made by the electrical bias varied between $F = \{-30$ kV/cm, $+30$ kV/cm$\}$. Figures 4(a) and 4(c) show the numerically calculated charge densities, $\rho_\chi(x,y,z_0) = |f^h_{0,\chi}(x,y,z_0)|^2$, of each χ component of the lowest hole state of the QD without and with an electric field, on the $z = z_0$ plane where the maximum of the major HH wave function is located. The lateral extent of the major HH lateral wave function, $f^h_\Downarrow(x,y,z_0)$, is seen to be shrunk by the positive bias, as indicated by Fig. 3(b).

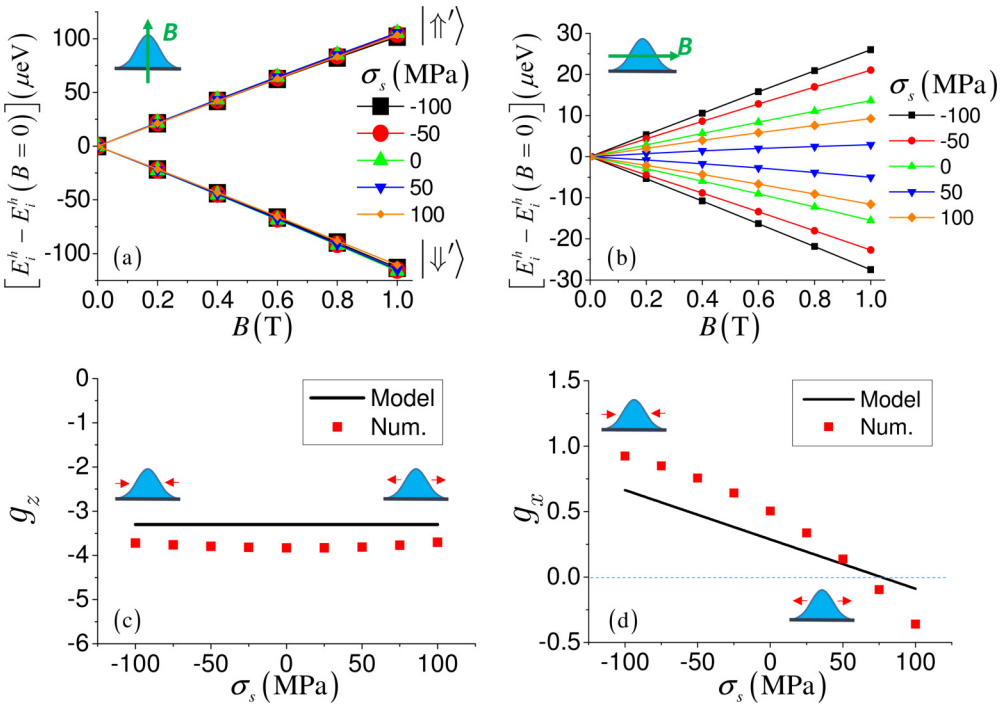

FIG. 2. (a) [(b)] Numerically calculated magnetoenergy spectra of the lowest hole spin-split states of the tall x-elongated GaAs/AlGaAs DE-QD with $H = 12$ nm, $\Lambda_x = 29.4$ nm, and $\Lambda_y = 19.6$ nm, under vertical magnetic fields $\vec{B} = (0,0,B)$ [in-plane magnetic fields $\vec{B} = (B,0,0)$] and uniaxially stressed by $\sigma_s = -100, \ldots 0, \ldots +100$ MPa along the x direction. (c) [(d)] The calculated longitudinal [transverse] effective g-factor, g_z [g_x], of the stressed QD versus σ_s, corresponding to the spin Zeeman splittings of (a) [(b)].

Corresponding to Figs. 3(a) and 3(b), the numerically calculated g_z and g_x, as functions of F, of the hole in the F-biased QD without stress ($\sigma_s = 0$) and with the uniaxial stress $\sigma_s = 70$ MPa are presented in Figs. 4(a) and 4(b), respectively. Overall, the longitudinal hole g-factors, g_z, are shown insensitive to the variation of F, while the transverse hole g-factors are significantly F-tunable. For comparison, the calculated g_x of a *flat* QD of $H = 6$ nm with the smaller degree of VBM is also presented [see the black line with square symbols in Fig. 4(b)]. In Fig. 4(b), a notable feature is that, in the absence of stress, the signs of the hole g_x-factors of the unstrained QDs cannot be reversed electrically even with the high bias field, $F = \pm 30$ kV/cm (see the black and blue lines for the flat and tall QDs, respectively) in spite of the significant F-driven change of the g_x by over 50% (from $g_x = 0.36$ to $g_x = 0.63$) for the tall QD. In contrast, with the uniaxial stress $\sigma_s = 70$ MPa at the experimentally accessible scale, the sign of the g_x-factor of the tall QD under the tensile stress can be reversed with a small bias field, $F \sim 10$ kV/cm [see the red line in Fig. 4(b)]. The model analysis presented below reveals an intrinsic obstacle for electrically reversing the sign of the g-factor for a single hole in a *unstressed* QD [12,14,15,19,23,24] and accounts for why in most existing experiments reversing the sign of a hole g-factor is technically so challenging [25,49].

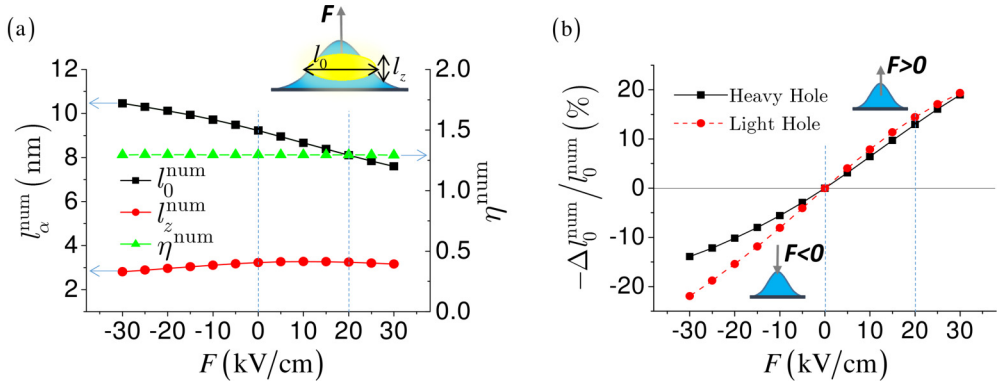

FIG. 3. (a) Numerically calculated lateral and vertical wave function extents, l_0^{num} and l_z^{num}, and (b) the inverse of the relative variation of the lateral wave function extent, $(-\Delta l_0^{num}/l_0^{num})$, of the major HH and the secondary LH components of the lowest hole state of the biased tall DE-QD considered in Fig. 2, versus the applied vertical electric fields F. One sees that the F-driven variations of the lateral extents of the HH- and LH-envelope functions are roughly proportional to F.

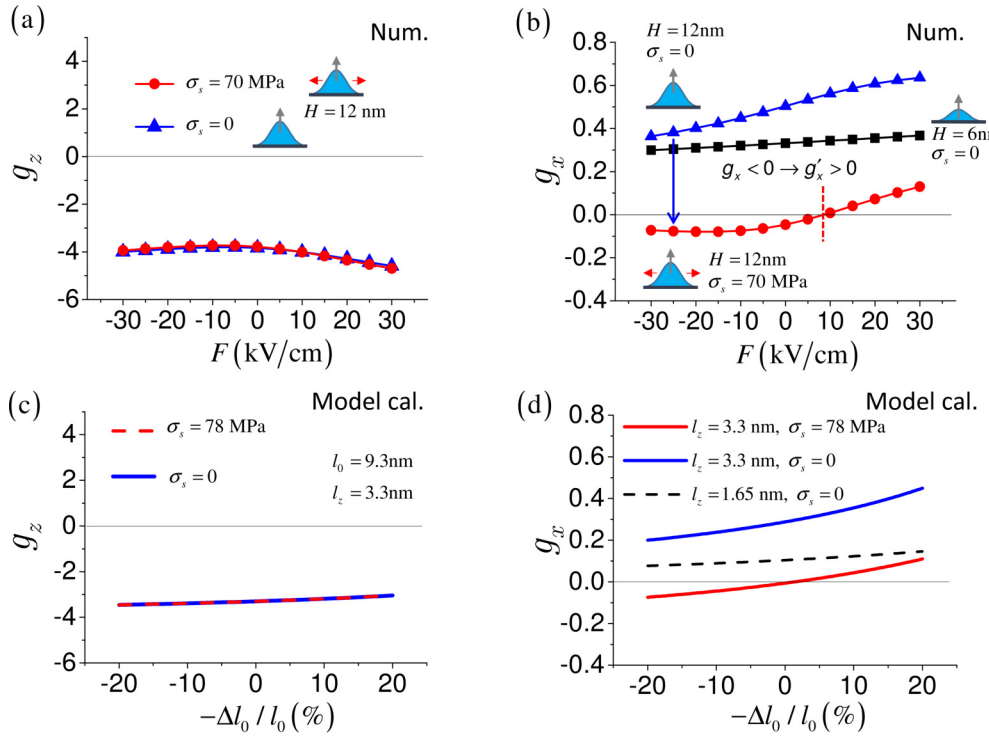

FIG. 4. (a) Numerically calculated longitudinal g_z and (b) transverse g_x factors versus the bias field F of a single hole in the biased tall QD of $H = 12$ nm without (blue triangles) and with (red circles) the uniaxial stress $\sigma_s = 70$ MPa. To highlight the VBM effect, the calculated g_x of a flat QD of $H = 6$ nm with the smaller degree of VBM is also presented [the back line with square symbols in (b)]. One notes that the sign of the g_x factor of the tall QD under the tensile stress can be reversed with a small bias field, $F \sim 10$ kV/cm. (c) The g_z and (d) the g_x factors calculated using Eq. (C6) and Eq. (9) based on the parabolic model for a single hole in a tall (flat) QD without and with the uniaxial stress $\sigma_s = 78$ MPa. The parameters of the hole wave function for the tall (flat) QD are $l_0 = 9.3$ nm $\times (1 \pm 20\%)$, $l_z = 3.3$ nm ($l_z = 1.65$ nm), where the relative l_0 variation, $(-\Delta l_0/l_0) = \{-20\%, +20\%\}$, corresponds to the variation of the electric field between $F = \{-30$ kV/cm, $+30$ kV/cm$\}$ [see Fig. 3(b)].

IV. ANALYSIS AND DISCUSSION

A. Model

For more analysis, we use the harmonic oscillation (HO) wave functions in the asymmetric 3D parabolic model to expand the undetermined envelope functions of the hole eigenstates of elongated DE-QDs, i.e., $f^h_{i,\chi}(\vec{r}) = \sum_n C_{i,\chi,n}\phi^\chi_n(\vec{r})$, where $\phi^\chi_n(\vec{r})$ denotes the HO basis labeled by $n = (n_x,n_y,n_z)$ with $n_\alpha = 0,1,2,3,\ldots$ in the spin-χ component of hole. The validity of the simple parabolic model for describing the low-lying states of DE-QDs has been confirmed by the previous theoretical and experimental studies [31]. Similar theoretical model was also adopted in Ref. [19] for studying the hole g-factors of electrically biased self-assembled InGaAs QDs but without applied stresses. Owing to the unequal effective masses of HH and LH, the spatial extents of the HH- and LH-envelope wave functions of finite-barrier QDs differ. We thus take the distinctive basis sets for expanding HH and LH wave functions, which are $\{\phi^{\Uparrow}_n\} = \{\phi^{\Downarrow}_n\} \equiv \{\phi^H_n\}$ and $\{\phi^{\uparrow}_{n'}\} = \{\phi^{\downarrow}_{n'}\} \equiv \{\phi^L_{n'}\}$, centered at $\vec{R}_H = (0,0,z_H)$ and $\vec{R}_L = (0,0,z_L)$, respectively. Throughout this work, we take the symbol of composite index, $n = (n_x,n_y,n_z)$, without a prime superscript [$n' = (n_x,n_y,n'_z)$ with a prime superscript] to specify the HO basis functions for HH [LH] wave functions. In the model, the lowest HO wave function for HH/LH is explicitly given by $\phi^{H/L}_{(000)}(\vec{r}) = \langle\vec{r}|000\rangle = \sqrt{\frac{1}{\pi^{3/2}l^{H/L}_x l^{H/L}_y l^{H/L}_z}}\exp\{-\frac{1}{2}[(\frac{x}{l^{H/L}_x})^2 + (\frac{y}{l^{H/L}_y})^2 + (\frac{z}{l^{H/L}_z})^2]\}$, in terms of the parameters of wave function extent, $\{l^{H/L}_{\alpha=x,y,z}\}$. The other excited HO wave function can be generated by successively applying the raising ladder operators onto the lowest state, as detailed in Appendix A.

By using the Lödwen perturbation theory and treating the HH-LH couplings as perturbations, the effective 2×2 Hamiltonian matrix for the lowest HH-like states of a QD with arbitrary $\vec{B}$ is derived and formulated as (see Appendix C for details)

$$H'_h = -\tfrac{1}{2}\mu_B\vec{\sigma}\cdot\mathbf{g_h}\cdot\vec{B}, \tag{6}$$

which is in the VBM-hole basis given by

$$|\Uparrow'\rangle \approx |\phi^H_0\rangle|\Uparrow\rangle + \sum_{n'}\gamma^*_{n'}|\phi^L_{n'}\rangle|\uparrow\rangle - \sum_{n'}\beta^*_{n'}|\phi^L_{n'}\rangle|\downarrow\rangle, \tag{7}$$

$$|\Downarrow'\rangle \approx |\phi^H_0\rangle|\Downarrow\rangle - \sum_{n'}\beta_{n'}|\phi^L_{n'}\rangle|\uparrow\rangle - \sum_{n'}\gamma_{n'}|\phi^L_{n'}\rangle|\downarrow\rangle, \tag{8}$$

where $\beta_{n'} \equiv \frac{R_{0,n'}}{\Delta^{HL}_{0,n'}}$ and $\gamma_{n'} \equiv \frac{S_{0,n'}}{\Delta^{HL}_{0,n'}}$ are the (complex) coefficients for the n'th HO basis in the corresponding LH components of a HH-like state, $S_{0,n'} \equiv \langle 0|S|n'\rangle = \int d^3r\,\phi^H_{(000)}{}^*\hat{S}\phi^L_{(n_x,n_y,n_z)'}$, $R_{0,n'} \equiv \langle 0|R|n'\rangle$, $\Delta^{HL}_{0,n'} \equiv E^L_{n'} - E^H_0 = E^L_{(n_x,n_y,n_z)'} - E^H_0$, $E^H_0 = \langle(000)|P+Q+V_{QD}|(000)\rangle$, $E^L_0 \equiv \langle(000)'|P-Q+V_{QD}|(000)'\rangle$,

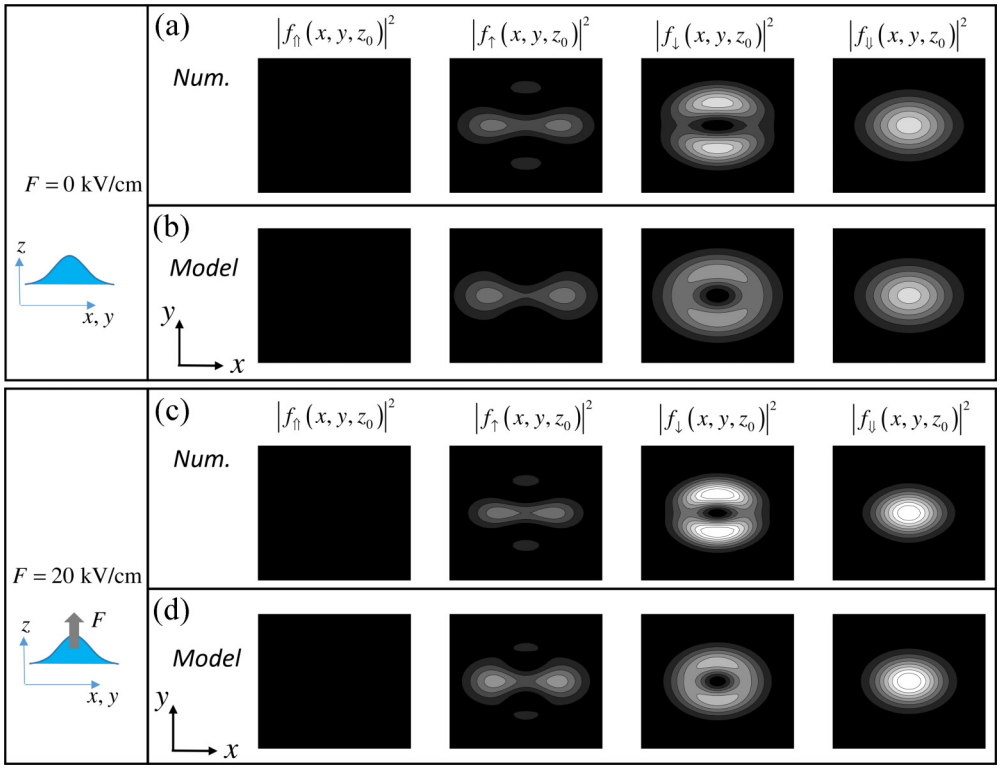

FIG. 5. (a) Numerically calculated charge densities, $\rho_\chi(x,y,z_0) = |f^h_\chi(x,y,z_0)|^2$, of each χ component of the lowest hole state of the elongated QD for Figs. 2 and 3 without external electric field, on the $z = z_0$ plane where the maximum of the major HH wave function is located. (b) Charge densities yielded by the formalisms of the parabolic model in Sec. IV and Table I, with the appropriately fitted parameters $\{l^{H/L}_\alpha\}$ (see text in Sec. IV). (c) [(d)] Charge densities that are calculated numerically [yielded by the model] of each χ component of the lowest hole state of the QD with a vertical electrical field $F = 20$ kV/cm.

and $\vec{\sigma} = (\sigma_x,\sigma_y,\sigma_z)$ represents the Pauli matrices; $\mathbf{g_h} = \mathrm{diag}(g_x,g_y,g_z)$ is defined as the effective g-tensor for the hole doublet. Here, for brevity we take $n = 0$ ($n' = 0'$) to label the lowest pure-HH (pure-LH) HO basis function, $\phi^{H/L}_0 = \phi^{H/L}_{(000)}$.

By diagonalizing Eq. (6) for a single hole in a QD with a $\vec{B}$-field, we solve the spin-split energy levels, the wave functions and the g-tensor of the hole, explicitly in terms of $\beta_{n'}$ and $\gamma_{n'}$. As a result, one can show that the longitudinal g_z-factor is mainly associated with $\gamma_{n'}$ while the transverse one is associated with $\beta_{n'}$, as detailed in Appendix C. For the QD considered in Figs. 2, 3, 5(a), and 5(c), we take the fitted parameters, $l^H_x = 10.6$ nm, $l^H_y = 8.2$ nm, $l^H_z = 3.3$ nm, $l^L_x = 9.1$ nm, $l^L_y = 7.0$ nm, $l^L_z = 4.5$ nm, and the misalignment of the HH- and LH-envelope wave functions, $\Delta z_{HL} = z_H - z_L = 1$ nm. The parameters of HH wave function extent $\{l^H_\alpha\}$ for the QDs studied in this work are determined by the best fitting of the numerically calculated envelope wave functions of the major HH component of the lowest HH-like states. The parameters $\{l^L_\alpha\}$ for the LH wave functions are inferred from $\{l^H_\alpha\}$ via the relationship, $l^L_\alpha = (m^H_\alpha/m^L_\alpha)^{1/4} \cdot l^H_\alpha$ where $\alpha = x,y,z$. With the fitted parameters, we calculate the few leading HO terms in Eqs. (7) and (8) using the formulations for $\beta_{n'}$ and $\gamma_{n'}$ in Table I and the algebraic method of HO in Appendix A. Then, from the solved eigenvector for Eq. (6) in the HO basis, we obtain the wave functions of each χ component of the lowest VBM hole state of the QD without and with a bias field, whose charge densities are plotted in Figs. 5(b) and 5(d), showing an excellent agreement with the fully numerical ones.

B. Sign reversibility of hole g-factors

For the purpose of g-TMR control, the transverse g_x-factor that shows sign reversible with tuning stresses is of interest and the main focus in our analysis. Taking the HO basis functions up to the d-shell and preserving the most leading terms in Eqs. (7) and (8), the transverse hole g_x-factor of a stressed QD under an in-plane magnetic field, $\vec{B} = (B,0,0)$, is derived as

$$g_x \approx a_{000}\beta_{000} + b_{000}\beta_{000} + b_{020}\beta_{020}, \tag{9}$$

where $a_{000} = -\frac{4}{\sqrt{3}}$, $b_{000} = 2\sqrt{6}\gamma_3(\lambda_{(000),(200)'} - \lambda_{(000),(002)'})$, and $b_{020} = -2\sqrt{6}(\gamma_3 - \gamma_2)\lambda_{(000),(000)'}$; $\lambda_{n,n'} \equiv \langle\phi^H_n|\phi^L_{n'}\rangle$ is the overlap between the HO basis functions for HH and LH. The nonorthogonality of ϕ^H_n and $\phi^L_{n'}$ leads to $\lambda_{n,n'} \neq 0$ even for $n \neq n'$ (see Appendix C). For brevity of formalisms, we neglect the anisotropy of QD and redefine the parameter $l_0 \equiv \sqrt{l^H_x l^H_y}$ (=9.3 nm) to measure the average lateral extent of wave function hereafter. The explicit formalisms of the leading β_n and γ_n, in terms of wave function extents, $\{l_\alpha\}$, and effective masses, $m^{H/L}_\alpha$, are listed in Table I. Equation (9) shows the correlation between the transverse hole g-factor and the VBM terms, β_{000} and β_{020}. The first term in Eq. (9) ($a_{000}\beta_{000}$) is due to the weak spin Zeeman term of Eq. (3). The latter two terms involving β_{000} and β_{020} are induced by the $\vec{B}$-induced vector potential $\vec{A}$ and dominate the electrical and strain-field-dependent features of the transverse g-factor.

TABLE I. Formulations of the leading β_n and γ_n in Eqs. (7) and (8), which are derived in the 3D parabolic model under the approximation $l_0 \equiv \sqrt{l_x^H l_y^H} \gg l_z \equiv l_z^H$. The anisotropic HH (LH) effective masses are $m_x^H = m_y^H = m_\parallel^H = \frac{1}{\gamma_1+\gamma_2}$ and $m_z^H = \frac{1}{\gamma_1-2\gamma_2}$ ($m_x^L = m_y^L = m_\parallel^L = \frac{1}{\gamma_1-\gamma_2}$ and $m_z^L = \frac{1}{\gamma_1+2\gamma_2}$). $\lambda_{nn'} \equiv \langle \phi_n^H | \phi_{n'}^L \rangle$.

$n = (n_x n_y n_z)$	β_n
(000)	$\beta_{000} = -\frac{1}{4} \frac{\lvert d \rvert S_{44} \sigma_s \lambda_{000,000'}}{\left(\frac{\hbar^2}{2m_0}\right)\left(\frac{1}{m_z^H}\right)\left(\frac{1}{l_z}\right)^2} \frac{\sqrt{m_z^L}}{\sqrt{m_z^H}-\sqrt{m_z^L}}$
(110)	$\beta_{110} = i\sqrt{2}\left(\frac{\gamma_2}{\gamma_3}\right)\beta_{020}$
(020)	$\beta_{020} = -\frac{\sqrt{6}}{2} \frac{\gamma_3}{\gamma_1-2\gamma_2} \left(\frac{l_z}{l_0}\right)^2 \frac{\sqrt{m_z^L}}{\sqrt{m_z^H}-\sqrt{m_z^L}} \sqrt{\frac{m_\parallel^L}{m_\parallel^H}} \left(\lambda_{000,000'} - 2\sqrt{2}\lambda_{000,200'}\right)$
$n = (n_x n_y n_z)$	γ_n
(100)	$\gamma_{100} = \frac{\sqrt{3}\gamma_3}{\gamma_1-2\gamma_2} \left(\frac{l_z}{l_0}\right) \frac{\sqrt{m_z^L}}{\sqrt{m_z^H}-\sqrt{m_z^L}} \left(\frac{m_z^L}{m_z^H}\right)^{\frac{1}{4}} \left(\frac{m_\parallel^L}{m_\parallel^H}\right)^{\frac{1}{4}} \lambda_{000,001'}$
(010)	$\gamma_{010} = (-i)\gamma_{100}$
(101)	$\gamma_{101} = -\frac{\sqrt{3}\gamma_3}{\gamma_1-2\gamma_2} \left(\frac{l_z}{l_0}\right) \frac{\sqrt{m_z^L}}{3\sqrt{m_z^H}-\sqrt{m_z^L}} \left(\frac{m_z^L}{m_z^H}\right)^{\frac{1}{4}} \left(\frac{m_\parallel^L}{m_\parallel^H}\right)^{\frac{1}{4}} (\lambda_{000,000'} - \sqrt{2}\lambda_{000,200'} - \sqrt{2}\lambda_{000,002'})$
(011)	$\gamma_{011} = (-i)\gamma_{101}$

Analytically, one can show that

$$\beta_{000}(\sigma_s) = -\frac{1}{4} \frac{\lvert d \rvert S_{44} \sigma_s \lambda_{000,000'}}{\left(\frac{\hbar^2}{2m_0}\right)\left(\frac{1}{m_z^H}\right)\left(\frac{1}{l_z}\right)^2} \frac{\sqrt{m_z^L}}{\sqrt{m_z^H}-\sqrt{m_z^L}} \propto \sigma_s, \quad (10)$$

$$\beta_{020}(F) = -\frac{\sqrt{6}}{2} \frac{\gamma_3}{\gamma_1-2\gamma_2} \left(\frac{l_z}{l_0}\right)^2 \frac{\sqrt{m_z^L}}{\sqrt{m_z^H}-\sqrt{m_z^L}} \times \sqrt{\frac{m_\parallel^L}{m_\parallel^H}} (\lambda_{000,000'} - 2\sqrt{2}\lambda_{000,200'}) \propto \frac{1}{l_0^2}. \quad (11)$$

The above equations show that β_{000} is tunable by stress σ_s while β_{020} is stress irrelevant but dependent on the electrically tunable l_0. From Eqs. (9) and (11), it is predicted that g_x-factor increases with increasing the vertical electrical field F acted on a QD (since greater F smaller l_0). The predicted F dependence of the g_x-factor is consistent with the analysis and computed results in Ref. [19]. Notably, the inverse quadratic dependence of β_{020} on electrically tunable l_0 indicates that, without any external stress $\sigma_s = 0$, it is hard to make the sign reversal of g_x by simply using electrical field. This accounts for why, in most existing experiments, electrically reversing the signs of hole g-factors for semiconductor nanostructures remains a challenging task [12,14,19,25].

According to the strong (weak) F dependence of the l_0 (l_z) shown in Fig. 3(a), we shall consider l_0 as the sole F-tunable parameter and treat l_z in the model analysis presented below. With a bias field varied from F to $F' = F + \Delta F$, leading to $l_0 \to l_0' = l_0 + \Delta l_0$, the g_x-factor of a hole in a biased QD under a constant stress is varied by $\Delta g_x = g_x(l_0') - g_x(l_0) \propto [\beta_{020}(l_0') - \beta_{020}(l_0)]$ according to Eqs. (9) and (11). Thus the electrical tunability of g_x-factor is measured by

$$\frac{\partial g_x}{\partial l_0} \propto \frac{\partial \beta_{(020)}}{\partial l_0} \equiv t_F = -\frac{2}{l_0} \beta_{(020)}, \quad (12)$$

being proportional to $\beta_{(020)}$.

To illustrate how the g-TMR scheme functions, let us reformulate Eq. (6) as

$$H_h' = -\frac{1}{2} \mu_B \vec{\sigma} \cdot \mathbf{g_h} \cdot \vec{B} \equiv -\hbar \frac{\vec{\sigma}}{2} \cdot \vec{\Omega}, \quad (13)$$

where a VBM hole in a QD under a magnetic field can be viewed as a pseudospin $\frac{\vec{\sigma}}{2}$ that is coupled to an effective field defined by

$$\vec{\Omega} \equiv (\Omega_x, \Omega_y, \Omega_z)^T = \frac{\mu_B}{\hbar} (g_x B_x, g_y B_y, g_z B_z)^T, \quad (14)$$

whose orientation is determined not only by that of the external $\vec{B}$ field but also by the anisotropy of the g-tensor components. In other words, if each of the g-tensor components could be changed, say from $\{g_{\alpha=x,y,z}\}$ to $\{g'_{\alpha=x,y,z}\}$, equivalently the resulting effective field is rotated from $\vec{\Omega}$ to $\vec{\Omega}'$ by a phase angle θ_Ω, as illustrated by Fig. 1(d). Following Ref. [11], a FSC is achievable if the effective field $\vec{\Omega}$ could be rotated by 90°, i.e., $\vec{\Omega} \cdot \vec{\Omega}' = 0$ or $\theta_\Omega = \frac{\pi}{2}$. Considering a magnetic field lying on the $x-z$ plane, $\vec{B} = (B_x, 0, B_z)$, the condition of FSC over the spin of the QD-confined hole under the B field is fulfilled with

$$g_x \cdot g_x' = -|g_z|^2 \tan^2 \theta_B < 0, \quad (15)$$

where $\theta_B \equiv \tan^{-1} \frac{B_z}{B_x}$ and that $g_z' \approx g_z$ is taken.

According to Eqs. (C6), (C8), (9), and Table I, we calculate the g_z- and g_x-factors of a hole in the biased tall [flat] QDs with the electrically varied $l_0 = 9.3$ nm $\times (1 \pm 20\%)$ as presented in Fig. 4(c) [4(d)], where $\Delta l_0 / l_0 = \pm 20\%$ correspond to $F = \mp 30$ kV/cm according to Fig. 3, and the parameters $l_0 = 9.3$ nm and $l_z = 3.3$ nm [1.65 nm] are taken. To reproduce the numerical data of the stressed QD presented in Figs. 3(c) and 3(d), the applied stress to the QD is set to be $\sigma_{s,op} \sim 78$ MPa that enables the sign reversal of the g_x-factor at the same small bias. Compared with the numerical results of Figs. 4(a) and 4(b), the model calculations well produce the F-dependent features of the longitudinal and transverse g-factors of the stressed and unstressed QDs, but slightly overestimate the magnitude of the critical stress, $\sigma_{s,op}$, that

makes the g_x-factor nearly vanishing and the optimal control over the sign of the g_x-factor.

To make a g_x-factor well tunable so as to reverse its sign, one naturally attempts to raise the electrical tunability, t_F. According to Eq. (12), this can be achieved by increasing the magnitude of $|\beta_{020}|$, which is greater in a taller QD [since $|\beta_{020}| \propto l_z^2$ according to Eq. (11)]. In Figs. 4(b) and 4(d), however, no such sign reversal of the g_x-factor happens for the un-stressed tall QD even as the applied bias field is driven over the wide range of $F = \pm 30$ kV/cm. This is because the greater $|\beta_{020}|$ of a taller QD leads to the greater magnitude of g_x-factor ($g_x \propto \beta_{020}$) as well and makes the sign switch even harder [see Eqs. (9), (11), and (12)].

To decrease the magnitude of g_x-factor and to make the sign reversal easier, we turn to considering a *flat* QD with $H = 6$ nm and the same side lengths. Indeed, as one expects, the numerically calculated g_x-factor [shown by the black line in Fig. 3(d)] of the flat QD is overall smaller than that of the tall QD but still cannot reverse its sign even with $F \sim \pm 30$ kV/cm (correspondingly, $\Delta l_0/l_0 \sim \mp 20\%$). This is because the degree of VBM in the flat QD is small and so is the resulting electrical tunability of g_x-factor, $t_F \propto \beta_{020}$ [see Eq. (12)]. The predicted size dependence of the transverse hole g-factor of the QD is consistent with the theoretical analysis for Fig. 4 in Ref. [19]. The simple analysis above accounts for why it is so difficult in most experiments to achieve the sign reversal of transverse g-tensor components by pure electrical means [14,16,17,19,25].

In turn, according to Eqs. (9) and (10), imposing a uniaxial stress onto a QD creates a stress-tunable component of β_{000} and can offset the transverse g-factor to be nearly zero if the applied stress is appropriate. Importantly, the application of a uniaxial stress can decrease the magnitude of the g_x-factor but does not affect the F tunability of g_x, t_F, which is associated with only the stress-irrelevant VBM, β_{020}, as shown in Eq. (12). The red line with filled circles in Fig. 4(b) shows the numerically calculated g_x-factor versus the applied F for the tall QD under a tensile uniaxial stress of 70 MPa. One sees that the g_x-factor of the unbiased QD is mechanically offset to nearly zero and, with keeping the same high F tunability, the sign of g_x-factor can be reversed by a small bias field $F \sim 10$ kV/cm [corresponding to a slight wave function variation, $|\Delta l_0^{\rm num}/l_0^{\rm num}| \sim 5\%$, as seen in Fig. 3(b)].

C. Stress-assisted full spin control

Finally, we shall extend the model analysis to explicitly derive the general FSC condition, in terms of F-driven wave function variation and the strength of stress, for a hole spin in a DE-QD. Following Eq. (14), the condition for a FSC over a hole spin in a F-bias QD under which the two F-switchable effective fields, $\vec{\Omega}$ and $\vec{\Omega}'$, are perpendicular to each other (i.e., $\theta_\Omega \equiv \cos^{-1} \frac{\vec{\Omega}\cdot\vec{\Omega}'}{|\vec{\Omega}||\vec{\Omega}'|} = \pi/2$) is derived as

$$\theta_\Omega = \cos^{-1} \frac{g_x g_x' + |g_z|^2 \tan^2\theta_B}{\sqrt{g_x^2 + |g_z|^2 \tan^2\theta_B}\sqrt{g_x'^2 + |g_z|^2 \tan^2\theta_B}} = \pi/2\,,$$

where a tilted magnetic field, $\vec{B} = (B_x, 0, B_z)$, is considered, $\theta_B \equiv \tan^{-1}\frac{B_z}{B_x}$, and $g_z = g_z'$ is taken.

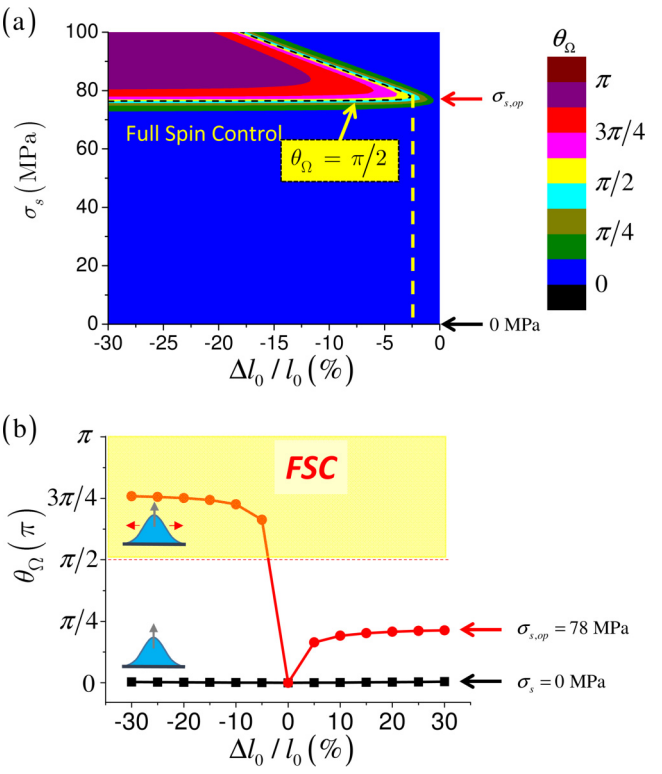

FIG. 6. (a) Contour plot of the calculated rotation angle θ_Ω of the effective field $\vec{\Omega}$ for a biased and stressed DE-QD within the parabolic model as a function of F-driven $\Delta l_0/l_0$ and the magnitude of the applied uniaxial stress σ_s. The condition for a full spin control (FSC) is $\theta_\Omega = \pi/2$. It is shown that a FSC is feasible only as the biased QD is stressed. (b) The calculated angles θ_Ω as functions of $\Delta l_0/l_0$ for the QD without stress ($\sigma_s = 0$) and with the optimal stress ($\sigma_{s,op} = 78$ MPa) that requires only a small wave function variation, $|\Delta l_0/l_0| \gtrsim 2.5\%$, for FSC (the regime highlighted in yellow).

In Fig. 6(a), the calculated angle θ_Ω of the F-rotated effective field for a hole spin in a stressed QD with $\theta_B = 0.1^\circ$ by electrical bias F is presented as a function of the F-induced $\Delta l_0/l_0$ and the stress σ_s. In the absence of stress ($\sigma_s = 0$, marked by the black horizontal arrow), the rotation angle of the effective field induced by F remains always too small ($\theta_\Omega \ll \pi/2$) to make a FSC. By contrast, a FSC (the yellow region where $\theta_\Omega = \pi/2$) is shown achievable with a small F-induced minimal wave function variation, $|\Delta l_0/l_0| \lesssim 5\%$ (corresponding to $F \sim 10$ kV/cm, far below the applied bias in the most existing experiments controlling g-factors), under the optimal stress $\sigma_{s,op} = 78$ MPa (marked by the red horizontal arrow) [25]. The constructive effect of mechanical stress on the controllability of the g-tensor and the resulting effective field is illustrated in Fig. 6(b) by the comparison of the calculated θ_Ω's as a function of the $\Delta l_0/l_0$ for the QD without stress ($\sigma_s = 0$) and with the critical stress ($\sigma_s = \sigma_{s,op}$). It is apparently seen that only the latter can make a FSC feasible.

V. SUMMARY

In summary, we have carried out a theoretical investigation of the g-factor tensors of single holes confined in droplet

epitaxial GaAs/AlGaAs QDs under electrical and mechanical controls within the four-band Luttinger-Kohn $\vec{k}\cdot\vec{p}$ model in both numerical and analytical manners. Our studies reveal and identify an intrinsic obstacle for a hole spin in a QD solely with electrical control to realize the scheme of electrical g-tensor modulations for a full spin coherent control. As a main constructive result, we show that, besides electrical gating, slightly stressing a QD can dramatically drop the magnitude of the required electrical bias for the sign reversal of the g-factor and makes feasible the full spin control over the QD-confined hole.

ACKNOWLEDGMENTS

The authors are grateful to the Ministry of Science and Technology of Taiwan (Contracts No. NSC-102-2112-M-009-009-MY2 and No. MOST 104-2112-M-009-002-MY2) and National Center for High-performance Computing (NCHC) of Taiwan, for financial and technical support. S.J.C. would like to thank Satoru Adachi (Hokkaido University), Reina Kaji (Hokkaido University), Takashi Kuroda (National Institute for Materials Science, Japan), Santosh Kumar (IFW, Dresden), and O. G. Schmidt (IFW, Dresden) for fruitful discussions.

APPENDIX A: 3D PARABOLIC MODEL

In the 3D parabolic model for a DE-QD, the confining potential for a pure HH or a pure LH in the dot is modeled by $V_{QD}^{\rm para}(x,y,z)=\Sigma_{\alpha=x,y,z}\frac{1}{2}m_\alpha^{H/L}(\omega_\alpha^{H/L})^2\alpha^2$, where $m_x^H=m_y^H=\frac{1}{\gamma_1+\gamma_2}$, $m_z^H=\frac{1}{\gamma_1-2\gamma_2}$, $m_x^L=m_y^L=\frac{1}{\gamma_1-\gamma_2}$, $m_z^L=\frac{1}{\gamma_1+2\gamma_2}$, and $m_\alpha^H(\omega_\alpha^H)^2=m_\alpha^L(\omega_\alpha^L)^2$ is fulfilled to make same the confining potential for HH and LH. In the model, the HO wave functions of a pure HH or a pure LH in a QD are solvable and taken in this work as basis functions for expanding the undetermined VBM hole states of QDs with the HH-LH couplings in the four-band $k\cdot p$ scheme. The lowest HO wave function for a pure HH/LH in the parabolic model is explicitly given by $\phi_{(000)}^{H/L}(\vec{r})=\langle\vec{r}|000\rangle=\sqrt{\frac{1}{\pi^{3/2}l_x^{H/L}l_y^{H/L}l_z^{H/L}}}\exp\{-\frac{1}{2}[(\frac{x}{l_x^{H/L}})^2+(\frac{y}{l_y^{H/L}})^2+(\frac{z}{l_z^{H/L}})^2]\}$, in terms of the parameters of wave function extent, $\{l_{\alpha=x,y,z}^{H/L}\}$, that are implicitly defined by $\omega_\alpha^{H/L}=\frac{\hbar}{m_\alpha^{H/L}}\frac{1}{(l_\alpha^{H/L})^2}$. Defining the ladder operators, $a_\alpha^\pm\equiv\frac{1}{\sqrt{2\hbar m_\alpha^{H/L}\omega_\alpha^{H/L}}}(m_\alpha^{H/L}\omega_\alpha^{H/L}\alpha\mp ip_\alpha)$ with $\alpha=x,y,z$, the other excited HO wave function can be generated by successively applying the operators onto the lowest HO state, i.e., $|\phi_{(n_x,n_y,n_z)}\rangle=(a_x^+)^{n_x}(a_y^+)^{n_y}(a_z^+)^{n_z}|000\rangle$, which follows the simple algebra $a_\alpha^+|n_\alpha\rangle=\sqrt{n_\alpha+1}|n_\alpha+1\rangle$ and $a_\alpha|n_\alpha\rangle=\sqrt{n_\alpha}|n_\alpha-1\rangle$. Reformulating the operators of linear momentum and position as $k_\alpha=i\sqrt{\frac{m_\alpha^L\omega_\alpha^L}{2\hbar}}(a_\alpha^+-a_\alpha)$ and $\alpha=\sqrt{\frac{\hbar}{2m_\alpha^L\omega_\alpha^L}}(a_\alpha^++a_\alpha)$, the full Hamiltonian of Eq. (1), as a function of $\vec{r}$ and $\vec{k}$, for a hole in a QD can be expressed in terms of $a_\alpha^\pm$, and enables us to carry out the analysis using the algebraic method.

APPENDIX B: GAUGE-INVARIANT DISCRETIZATION METHOD

To solve the multiband Schrödinger equation, $H_h|\psi_i^h\rangle=E_i^h|\psi_i^h\rangle$, based on Eq. (1) for a single hole in a QD with a magnetic field, we employ the gauge-invariant discretization method established by Refs. [38–41]. In the implementation of the theory, we first discretize the hole envelope wave in the real space functions in a set of uniform rectangular grids, denoted by $\{(x_i,y_j,z_k)\}$ with $i=0,1,2,\ldots,N_x$, $j=0,1,2,\ldots,N_y$, and $k=0,1,2,\ldots,N_z$, uniformly spaced by $x_{i+1}-x_i\equiv\Delta x$, $y_{j+1}-y_j\equiv\Delta y$, and $z_{k+1}-z_k\equiv\Delta z$, respectively. For high accuracy of the numerical method, the number of the grids should be set great enough to ensure the wave functions approaching nearly zero at the terminal grids ($i,j,k=0$, N_x, N_y, or N_z), and the spacings between grids as small as possible to minimize the interpolation errors. In the computations for the elongated QDs, we take the rectangular grids $80\times60\times96$ for a rectangular volume, 80 nm × 60 nm × 24 nm, which contains the computed QD at the center position. Following the theory in the finite difference scheme, an envelope wave function under the successive action of generalized differential operators is approximated by

$$\hat{D}_\alpha^2 f_{i,j,k}\approx\frac{1}{(\Delta\alpha)^2}\big[U_{i,j,k}^{\hat{s}_\alpha}f_{(i,j,k)+\hat{s}_\alpha}-2f_{i,j,k}+U_{i,j,k}^{-\hat{s}_\alpha}f_{(i,j,k)-\hat{s}_\alpha}\big],\tag{B1}$$

$$\begin{aligned}\hat{D}_\alpha\hat{D}_\beta f_{i,j,k}\approx\frac{1}{4\Delta\alpha\Delta\beta}\big[&U_{(ijk)+\hat{s}_\alpha}^{\hat{s}_\beta}U_{i,j,k}^{\hat{s}_\alpha}f_{(ijk)+\hat{s}_\alpha+\hat{s}_\beta}\\&-U_{(ijk)+\hat{s}_\alpha}^{-\hat{s}_\beta}U_{i,j,k}^{\hat{s}_\alpha}f_{(ijk)+\hat{s}_\alpha-\hat{s}_\beta}\\&-U_{(ijk)-\hat{s}_\alpha}^{\hat{s}_\beta}U_{i,j,k}^{-\hat{s}_\alpha}f_{(ijk)-\hat{s}_\alpha+\hat{s}_\beta}\\&+U_{(ijk)-\hat{s}_\alpha}^{-\hat{s}_\beta}U_{i,j,k}^{-\hat{s}_\alpha}f_{(ijk)-\hat{s}_\alpha-\hat{s}_\beta}\big],\end{aligned}\tag{B2}$$

where $f_{(i,j,k)}\equiv f(x_i,y_j,z_k)$, $\alpha,\beta=x,y,z$, $\hat{s}_x=(1,0,0)$, $\hat{s}_y=(0,1,0)$, $\hat{s}_z=(0,0,1)$, and

$$U_{i,j,k}^{\pm\hat{s}_\alpha}=\exp\left[-i\frac{e}{\hbar}\frac{1}{2}(A_{\alpha,(i,j,k)}+A_{\alpha,(i,j,k)\pm\hat{s}_\alpha})(\pm\Delta\alpha)\right].\tag{B3}$$

As examples of Eqs. (B1) and (B2), $\hat{D}_x^2 f_{i,j,k}$ and $\hat{D}_x\hat{D}_y f_{i,j,k}$ are, respectively, approximated by

$$\hat{D}_x^2 f_{i,j,k}\approx\frac{1}{(\Delta x)^2}\big[U_{(i,j,k)}^{(1,0,0)}f_{(i+1,j,k)}-2f_{(i,j,k)}+U_{(i,j,k)}^{(-1,0,0)}f_{(i-1,j,k)}\big],\tag{B4}$$

$$\begin{aligned}\hat{D}_x\hat{D}_y f_{i,j,k}\approx\frac{1}{4\Delta x\Delta y}\big[&U_{(i+1,j,k)}^{(0,1,0)}U_{(i,j,k)}^{(1,0,0)}f_{(i+1,j+1,k)}\\&-U_{(i+1,j,k)}^{(0,-1,0)}U_{(i,j,k)}^{(1,0,0)}f_{(i+1,j-1,k)}\\&-U_{(i-1,j,k)}^{(0,1,0)}U_{(i,j,k)}^{(-1,0,0)}f_{(i-1,j+1,k)}\\&+U_{(i-1,j,k)}^{(0,-1,0)}U_{(i,j,k)}^{(-1,0,0)}f_{(i-1,j-1,k)}\big].\end{aligned}\tag{B5}$$

Figures 7(a) and 7(b) schematically illustrate the first terms in Eqs. (B4) and (B5), respectively.

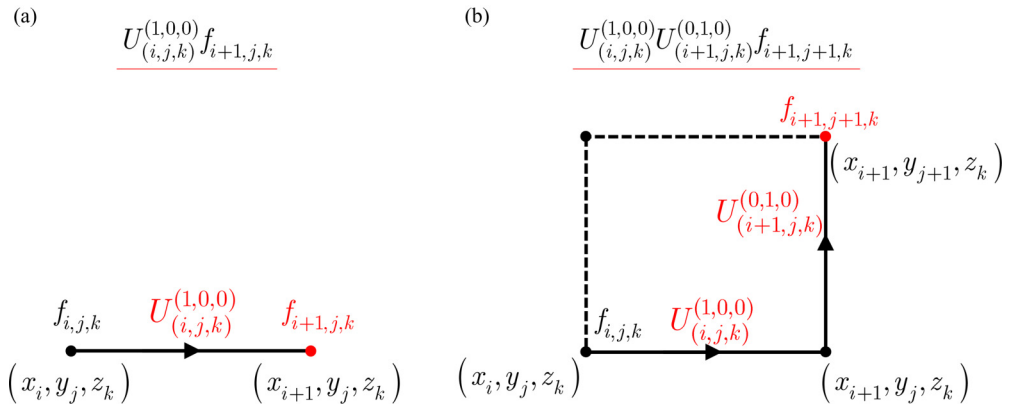

FIG. 7. Schematic illustration for computing the first term, (a) $\hat{D}_x^2 f_{i+1,j,k}$, in Eq. (B4) and (b) $\hat{D}_x \hat{D}_y f_{i+1,j+1,k}$ in Eq. (B5) in the gauge-invariant discretization method [38–41].

APPENDIX C: MODEL ANALYSIS FOR HOLE EIGENSTATES AND g-FACTORS

Using the Löwden perturbation theory, one can reduce the Hamiltonian matrix of Eq. (1) in the complete product basis of HO functions and the Bloch functions to an effective 2×2 Hamiltonian matrix for the lowest hole doublet of a QD with a magnetic field, as derived as

$$H'_h = \begin{pmatrix} H'_{\Uparrow'\Uparrow'} & H'_{\Uparrow'\Downarrow'} \\ H'_{\Downarrow'\Uparrow'} & H'_{\Downarrow'\Downarrow'} \end{pmatrix}, \tag{C1}$$

with

$$H'_{\Uparrow'\Uparrow'} = E_0^H - \mu_B B_z - \sum_{i'} \frac{|S_{0,i'}|^2 + |R_{0,i'}|^2}{\Delta^{HL}_{0,i'}}, \tag{C2}$$

$$H'_{\Downarrow'\Downarrow'} = E_0^H + \mu_B B_z - \sum_{n'} \frac{|S^\dagger_{0,n'}|^2 + |R^\dagger_{0,n'}|^2}{\Delta^{HL}_{0,n'}}, \tag{C3}$$

$$H'_{\Uparrow'\Downarrow'} = \frac{\mu_B (B_x - i B_y)}{\sqrt{3}} \frac{R_{0,0'} + (R^\dagger)_{0,0'}}{\Delta^{HL}_{0,0'}} - \sum_{n'} \frac{-S_{0,n'}(R^\dagger_{0,n'})^* + R_{0,n'}(S^\dagger_{0,n'})^*}{\Delta^{HL}_{0,n'}}. \tag{C4}$$

Under the perturbation treatment, the HH-like basis, $|\Uparrow'\rangle$ and $|\Downarrow'\rangle$, for the effective hole Hamiltonian Eq. (C1) are expanded as Eqs. (7) and (8), with the VBM coefficients given by $\beta_{n'} \equiv \frac{R_{0,n'}}{\Delta^{HL}_{0,n'}}$ and $\gamma_{n'} \equiv \frac{S_{0,n'}}{\Delta^{HL}_{0,n'}}$. In the 3D parabolic model, the matrix elements of Eqs. (C2)–(C4), and the VBM coefficients in Eqs. (7) and (8) can be derived as functions of the QD parameters, $\{l_\alpha\}$, the hole effective masses, and the magnetic field. Taking only the few leading terms in Eqs. (7) and (8) (as listed in Table I), the eigenstates, energies, and the resulting g-factor of a hole in a QD with a magnetic field can be computed seminumerically or even analytically, as presented below.

1. Longitudinal magnetic field

Substituting ($\vec{B} = (0,0,B_z)$) into Eqs. (C1)–(C4), one derives the effective Hamiltonian for the lowest hole doublet of a QD in a longitudinal magnetic field,

$$H'_h(\vec{B} = (0,0,B_z)) = \begin{pmatrix} H'_{\Uparrow'\Uparrow'} & 0 \\ 0 & H'_{\Downarrow'\Downarrow'} \end{pmatrix} \equiv -g_z \mu_B B_z \frac{\sigma_z}{2}, \tag{C5}$$

from which the effective g_z-factor is implicitly defined, and after some algebra derived as

$$g_z \approx 2 - 4\sqrt{3}\gamma_3 \left(\frac{l_0}{l_z}\right)\left(\frac{m_z^L}{m_z^H}\right)^{\frac{1}{4}}\left(\frac{m_\parallel^H}{m_\parallel^L}\right)^{\frac{1}{4}} \times [\lambda_{(000),(001)'}\gamma_{100} - (\lambda_{(000),(000)'} + \sqrt{2}\lambda_{(000),(200)'} - \sqrt{2}\lambda_{(000),(002)'})\gamma_{101}], \tag{C6}$$

where $\lambda_{0,n'} \equiv \langle \phi_0^H | \phi_{n'}^L \rangle$ is the overlap between the HO-wave functions for HH and LH. In the derivation of the g-tensor for a hole in a QD with $\vec{B}$, we expand $\beta_{n'}$ and $\gamma_{n'}$ as functions of $\vec{B}$ up to the linear term of B_α, neglect the other higher order terms of B, and take the approximation that $l_x = l_y \equiv l_0$ and $l_z \ll l_0$. Under the simplifications, the few leading β_n and γ_n as functions of l_0 and l_z are summarized in Table I. For the QDs studied in this work, we consider the misalignment of the HH and LH wave functions, $\Delta z_{HL} = z_H - z_L = 1$ nm, which leads to nonvanishing $\lambda_{0,n'} = \int d^3r\, \phi^H_{(000)}{}^* \phi^L_{(n_x,n_y,n_z)'}$ for $n \neq 0$.

2. Transverse magnetic field

For $\vec{B} = (B_x,0,0)$, we derive the effective hole Hamiltonian as

$$H'_h(\vec{B} = (B_x,0,0)) = \begin{pmatrix} 0 & H'_{\Uparrow'\Downarrow'} \\ H'_{\Downarrow'\Uparrow'} & 0 \end{pmatrix} \equiv -\tilde{g}_x \mu_B B_x \frac{\sigma_x}{2} \tag{C7}$$

from which the effective g_x-factor is derived as

$$g_x \approx \left[-\frac{4}{\sqrt{3}} + 2\sqrt{6}\gamma_3(\lambda_{(000),(200)'} - \lambda_{(000),(002)'})\right]\beta_{000} + 2\sqrt{6}\lambda_{(000),(000)'}(\gamma_3 - \gamma_2)(-\beta_{(020)}), \tag{C8}$$

where $l_x = l_y \equiv l_0$ and $l_z \ll l_0$ is assumed. Equation (C8) is rewritten as Eq. (9) in the main text.

[1] R. Hanson, L. P. Kouwenhoven, J. R. Petta, S. Tarucha, and L. M. K. Vandersypen, Rev. Mod. Phys. **79**, 1217 (2007).

[2] D. Loss and D. P. DiVincenzo, Phys. Rev. A **57**, 120 (1998).

[3] F. H. L. Koppens, C. Buizert, K. J. Tielrooij, I. T. Vink, K. C. Nowack, T. Meunier, L. P. Kouwenhoven, and L. M. K. Vandersypen, Nature (London) **442**, 766 (2006).

[4] J. R. Petta, A. C. Johnson, J. M. Taylor, E. A. Laird, A. Yacoby, M. D. Lukin, C. M. Marcus, M. P. Hanson, and A. C. Gossard, Science **309**, 2180 (2005).

[5] Y. Tokura, W. G. van der Wiel, T. Obata, and S. Tarucha, Phys. Rev. Lett. **96**, 047202 (2006).

[6] M. Pioro-Ladrière, T. Obata, Y. Tokura, Y.-S. Shin, T. Kubo, K. Yoshida, T. Taniyama, and S. Tarucha, Nat. Phys. **4**, 776 (2008).

[7] V. N. Golovach, M. Borhani, and D. Loss, Phys. Rev. B **74**, 165319 (2006).

[8] K. C. Nowack, F. H. L. Koppens, Y. V. Nazarov, and L. M. K. Vandersypen, Science **318**, 1430 (2007).

[9] S. Nadj-Perge, S. M. Frolov, E. P. A. M. Bakkers, and L. P. Kouwenhoven, Nature (London) **468**, 1084 (2010).

[10] Y. Kato, R. C. Myers, D. C. Driscoll, A. C. Gossard, J. Levy, and D. D. Awschalom, Science **299**, 1201 (2003).

[11] J. Pingenot, C. E. Pryor, and M. E. Flatté, Appl. Phys. Lett. **92**, 222502 (2008).

[12] T. Nakaoka, S. Tarucha, and Y. Arakawa, Phys. Rev. B **76**, 041301 (2007).

[13] J. Pingenot, C. E. Pryor, and M. E. Flatté, Phys. Rev. B **84**, 195403 (2011).

[14] R. S. Deacon, Y. Kanai, S. Takahashi, A. Oiwa, K. Yoshida, K. Shibata, K. Hirakawa, Y. Tokura, and S. Tarucha, Phys. Rev. B **84**, 041302 (2011).

[15] V. Jovanov, T. Eissfeller, S. Kapfinger, E. C. Clark, F. Klotz, M. Bichler, J. G. Keizer, P. M. Koenraad, G. Abstreiter, and J. J. Finley, Phys. Rev. B **83**, 161303 (2011).

[16] S. Takahashi, R. S. Deacon, A. Oiwa, K. Shibata, K. Hirakawa, and S. Tarucha, Phys. Rev. B **87**, 161302 (2013).

[17] N. Ares, V. N. Golovach, G. Katsaros, M. Stoffel, F. Fournel, L. I. Glazman, O. G. Schmidt, and S. D. Franceschi, Phys. Rev. Lett. **110**, 046602 (2013).

[18] N. Ares, G. Katsaros, V. N. Golovach, J. J. Zhang, A. Prager, L. I. Glazman, O. G. Schmidt, and S. D. Franceschi, Appl. Phys. Lett. **103**, 263113 (2013).

[19] J. H. Prechtel, F. Maier, J. Houel, A. V. Kuhlmann, A. Ludwig, A. D. Wieck, D. Loss, and R. J. Warburton, Phys. Rev. B **91**, 165304 (2015).

[20] A. Greilich, S. G. Carter, D. Kim, A. S. Bracker, and D. Gammon, Nat. Photon. **5**, 702 (2011).

[21] R. J. Warburton, Nat. Mater. **12**, 483 (2013).

[22] J. H. Prechtel, A. V. Kuhlmann, J. Houel, A. Ludwig, S. R. Valentin, A. D. Wieck, and R. J. Warburton, Nat. Mater. **15**, 981 (2016).

[23] A. Schwan, Appl. Phys. Lett. **99**, 221914 (2011).

[24] T. M. Godden, J. H. Quilter, A. J. Ramsay, Y. Wu, P. Brereton, I. J. Luxmoore, J. Puebla, A. M. Fox, and M. S. Skolnick, Phys. Rev. B **85**, 155310 (2012).

[25] A. J. Bennett, M. A. Pooley, Y. Cao, N. Sköld, I. Farrer, D. A. Ritchie, and A. J. Shields, Nat. Commun. **4**, 1522 (2013).

[26] N. Koguchi, S. Takahashi, and T. Chikyow, J. Cryst. Growth **111**, 688 (1991).

[27] J. M. Luttinger and W. Kohn, Phys. Rev. **97**, 869 (1955).

[28] M. Grundmann, O. Stier, and D. Bimberg, Phys. Rev. B **52**, 11969 (1995).

[29] D. Bimberg, N. N. Ledentsov, M. Grundmann, N. Kirstaedter, O. G. Schmidt, M. H. Mao, V. M. Ustinov, A. Y. Egorov, A. E. Zhukov, P. S. Kopev, Zh. I. Alferov, S. S. Ruvimov, U. Gösele, and J. Heydenreich, Phys. Status Solidi B **194**, 159 (1996).

[30] T. Kuroda, T. Mano, N. Ha, H. Nakajima, H. Kumano, B. Urbaszek, M. Jo, M. Abbarchi, Y. Sakuma, K. Sakoda, I. Suemune, X. Marie, and T. Amand, Phys. Rev. B **88**, 041306(R) (2013).

[31] Y.-H. Liao, C.-C. Liao, C.-H. Ku, Y.-C. Chang, S.-J. Cheng, M. Jo, T. Kuroda, T. Mano, M. Abbarchi, and K. Sakoda, Phys. Rev. B **86**, 115323 (2012).

[32] N. Ha, T. Mano, Y. L. Chou, Y. N. Wu, S. J. Cheng, J. Bocquel, P. M. Koenraad, A. Ohtake, Y. Sakuma, K. Sakoda, and T. Kuroda, Phys. Rev. B **92**, 075306 (2015).

[33] H. M. G. A. Tholen, J. S. Wildmann, A. Rastelli, R. Trotta, C. E. Pryor, E. Zallo, O. G. Schmidt, P. M. Koenraad, and A. Y. Silov, Phys. Rev. B **94**, 245301 (2016).

[34] A. Ulhaq, Q. Duan, E. Zallo, F. Ding, O. G. Schmidt, A. I. Tartakovskii, M. S. Skolnick, and E. A. Chekhovich, Phys. Rev. B **93**, 165306 (2016).

[35] J. D. Plumhof, V. Křápek, F. Ding, K. D. Jöns, R. Hafenbrak, P. Klenovský, A. Herklotz, K. Dörr, P. Michler, A. Rastelli, and O. G. Schmidt, Phys. Rev. B **83**, 121302(R) (2011).

[36] S. Kumar, E. Zallo, Y. H. Liao, P. Y. Lin, R. Trotta, P. Atkinson, J. D. Plumhof, F. Ding, B. D. Gerardot, S. J. Cheng, A. Rastelli, and O. G. Schmidt, Phys. Rev. B **89**, 115309 (2014).

[37] R. Trotta, E. Zallo, C. Ortix, P. Atkinson, J. D. Plumhof, J. van den Brink, A. Rastelli, and O. G. Schmidt, Phys. Rev. Lett. **109**, 147401 (2012).

[38] C. E. Pryor and M. E. Flatté, Phys. Rev. Lett. **96**, 026804 (2006).

[39] T. Andlauer, R. Morschl, and P. Vogl, Phys. Rev. B **78**, 075317 (2008).

[40] T. Andlauer and P. Vogl, Phys. Rev. B **79**, 045307 (2009).

[41] J. van Bree, A. Y. Silov, P. M. Koenraad, M. E. Flatté, and C. E. Pryor, Phys. Rev. B **85**, 165323 (2012).

[42] N. Levy, S. A. Burke, K. L. Meaker, M. Panlasigui, A. Zettl, F. Guinea, A. H. C. Neto, and M. F. Crommie, Science **329**, 544 (2010).

[43] M. C. Rechtsman, J. M. Zeuner, A. Tünnermann, S. Nolte, M. Segev, and A. Szameit, Nat. Photon. **7**, 153 (2013).

[44] J. M. Luttinger, Phys. Rev. **102**, 1030 (1956).

[45] S. L. Chuang, *Physics of Photonic Devices* (Wiley, New York, 2009).

[46] J. G. Keizer, J. Bocquel, P. M. Koenraad, T. Mano, T. Noda, and K. Sakoda, Appl. Phys. Lett. **96**, 062101 (2010).

[47] I. Toft and R. T. Phillips, Phys. Rev. B **76**, 033301 (2007).

[48] R. Kaji, T. Hozumi, Y. Hachiyama, T. Tomii, H. Sasakura, M. Jo, and S. Adachi, Appl. Phys. Express **7**, 065002 (2014).

[49] A. Srinivasan, K. L. Hudson, D. Miserev, L. A. Yeoh, O. Klochan, K. Muraki, Y. Hirayama, O. P. Sushkov, and A. R. Hamilton, Phys. Rev. B **94**, 041406 (2016).